Original Article

Development of a 3D-printed pelvic CT phantom combined with fresh pathological tissues of bone tumor

Xiaomin Li[1#], Bing Wu[1#], Yixuan Zou[2^], Guozhi Zhang[2^], Siyu Liu[1], Lulu Zhao[1], Zhengjia Zhang[1], Wen Wu[3], Chenglei Liu[1], Songtao Ai[1]

[1]Department of Radiology, Shanghai Ninth People's Hospital, Shanghai Jiao Tong University School of Medicine, Shanghai, China; [2]United Imaging Healthcare, Shanghai, China; [3]Department of Orthopedic Surgery, Shanghai Key Laboratory of Orthopedic Implants, Shanghai Ninth People's Hospital, Shanghai Jiao Tong University School of Medicine, Shanghai, China

Contributions: (I) Conception and design: S Ai, C Liu; (II) Administrative support: S Ai, W Wu; (III) Provision of study materials or patients: X Li, B Wu, W Wu; (IV) Collection and assembly of data: X Li, B Wu, Y Zou; (V) Data analysis and interpretation: X Li, B Wu, Y Zou, G Zhang; (VI) Manuscript writing: All authors; (VII) Final approval of manuscript: All authors.

[#]These authors contributed equally to this work.

Correspondence to: Prof. Songtao Ai. Department of Radiology, Shanghai Ninth People's Hospital, Shanghai Jiao Tong University School of Medicine, No. 639, Zhizaoju Road, Huangpu District, Shanghai, China. Email: aistss1024@sjtu.edu.cn; Prof. Chenglei Liu. Department of Radiology, Shanghai Ninth People's Hospital, Shanghai Jiao Tong University School of Medicine, No. 639, Zhizaoju Road, Huangpu District, Shanghai, China. Email: Lcl1984@aliyun.com.

Background: Computed tomography (CT) imaging is the most important and common means of detecting and diagnosing pelvic bone tumors. While phantoms with sufficient flexibility and anatomical realism are useful in CT research, using phantoms has been difficult for pelvic bone tumors because of the tumors' relatively large size and highly variable shape. By combining medical 3D printing technology and fresh tumor specimens, this study aimed to design such a hybrid phantom, test its imaging properties, and demonstrate its usefulness in optimizing the CT protocols.

Methods: Two phantoms were designed for 2 patients with pelvic bone tumors who underwent surgical resection. One phantom was scanned with a routine pelvic CT protocol and compared against the patient image to test the imaging properties. We optimized the imaging protocol by assessing a series of varied settings on tube voltage (80, 100, 120, and 140 kVp), tube current (80, 120, and 160 to 200 mAs), and pitch factor (0.5, 0.8, 1.1, and 1.4) using the other phantom. These were assessed in comparison to the clinical reference of 140 kVp, 240 mAs, and 1.0 pitch, respectively. Image quality was quantified in terms of CT value, image noise, signal to noise ratio (SNR), and contrast to noise ratio (CNR) in various regions of interest.

Results: With the routine protocol, the phantom image showed no significant difference in CT values of the bone and soft tissues and image noise compared to the patient image (all P values >0.05). With a lower tube voltage (80, 100, and 120 kVp) than the reference protocol, the CT value of bone tissue showed significant differences (all P values <0.001). No significant difference was found when applying a reduced tube current (all P values >0.05). With an increased helical pitch, pitches of 0.5, 0.8 and 1.1 were found to be comparable to those using the reference protocol (all P values >0.05).

Conclusions: The 3D-printed phantom can simulate the radiological properties of tumors in the pelvis and was successfully used in imaging studies of pelvic bone tumors. According to our preliminary findings, a low-dose pelvic CT protocol with acceptable image quality is achievable using reduced tube current or increased pitch.

---

^ ORCID: Yixuan Zou, 0000-0003-2916-3180; Guozhi Zhang, 0000-0002-4819-3580.

Quant Imaging Med Surg 2022;12(9):4647-4657 | https://dx.doi.org/10.21037/qims-22-147

Keywords: 3D printing; pelvic phantom; computed tomography; pelvic bone tumor; imaging protocol

Submitted Feb 15, 2022. Accepted for publication Jun 17, 2022.
doi: 10.21037/qims-22-147
View this article at: https://dx.doi.org/10.21037/qims-22-147

Introduction

Pelvic bone tumors account for about 3–4% of primary bone tumors, most of which are malignant. The irregular tumor shape and complex anatomical structure of the pelvis make it difficult to detect these tumors in their early stage (1-4). The wide invasive range of such tumors also leads to a high mortality and disability rate during an operation (5). Computed tomography (CT) is a common method for diagnosing pelvic bone tumors and surgical planning. However, even with CT, the preoperative assessment of these tumors remains a troublesome task because pelvic CT images are often associated with a mixture of obvious noise and artifacts due to the anatomical complexity and the heterogeneous X-ray–attenuating property of the pelvic region (6,7). Applying a higher tube voltage and/or tube current might help reduce the noise and artifacts, but it also increases the radiation dose to patients. Since gonadal tissues located within the pelvic region are highly sensitive to ionizing radiation, an excessive dose can induce serious genital system complications, such as chromosomal and sperm aberrations. Therefore, it is crucial to optimize CT acquisition protocols according to the fundamental principle of radiation protection; i.e., as low as reasonably achievable (ALARA), without compromising the diagnostic accuracy. Since it is not practical to repeat patient scans with different CT protocols, developing a pelvic phantom for bone tumors might be a viable approach to optimizing CT scan parameters and improving CT image quality.

Phantoms, as human body substitutes, are widely used in the quality assurance assessment of CT scanners in the measurement of associated radiation dose and in the education and training of technicians operating the imaging equipment (8-10). With the development of tissue-equivalent materials and computer technology, physical phantoms composed of simple geometry have evolved into anthropomorphic stylized phantoms, voxel phantoms, and boundary-representation phantoms, where the anatomical structures become increasingly realistic (11-15). However, the currently available phantoms have significant limitations for commercial or research purposes (16). First, most of these phantoms are relatively expensive and bulky. Second, homogeneous phantoms designed for radiation standardization and calibration lack anatomical details, whereas anatomical phantoms lack standardization, sometimes leading to inconsistent results. Third, finished phantoms lack the flexibility for variable configuration, for which the assessment of imaging methods and diseases is often limited.

Direct use of *in vitro* pathological specimens in CT imaging would be a way to acquire sufficient radiological properties of lesions. However, this approach is infeasible for pelvic bone tumors because the tumors' enormous volumes and variable shapes make it difficult to hold and fix for CT imaging. Moreover, fresh specimens are difficult to maintain over time, while long-term preserved specimens may lose their radiological attenuation attributes due to dehydration.

Reports show that medical 3D-printing technology can be used to create anthropomorphic phantoms. 3D-printed materials can mimic structural and mechanical properties of the tissues and organs, and anatomical structures can be printed from 3D images acquired using CT or magnetic resonance imaging (MRI) (17,18). However, 3D-printed materials still have some differences from real human tissue in terms of imaging properties. For instance, Niebuhr *et al.* (19) used 3D-printed materials to construct a pelvic phantom. Two of these materials, Agarose gels loaded with sodium fluoride (NaF) and a gadolinium-based contrast agent, showed good results when simulating various soft tissue properties in CT and MRI, but the salt-loaded gels led to severe artifacts in MRI.

We chose to design a hybrid pelvic phantom combining 3D printing and real bone tumors to circumvent these difficulties. The 3D-printing component uses patient-specific CT image data for defining the pelvic shape and uses low-cost materials with the equivalent X-ray attenuation of soft tissue. The tumor part is realized by placing fresh specimens in a preserved space within the phantom. This study aimed to make such a phantom, test its imaging properties with routine pelvic CT, and demonstrate its usefulness in optimizing CT protocols. We present the following article in accordance with the Materials Design Analysis Reporting (MDAR) checklist

Table 1 Sample patient characteristics

Characteristics	Patient A	Patient B
Age (years)	26	58
Gender	Male	Female
Pelvic size (diameter × height, cm^2)	37.0×18.5	36.0×22.0
Tumor size (width × length × height, cm^3)	8.5×8.2×11.0	7.8×12.5×11.5
Diagnosis	Osteochondroma	Chondrosarcoma
Enneking's classification	I	II and III
Surgery performed	Excision	Excision and endoprosthetic replacement

(available at https://qims.amegroups.com/article/view/10.21037/qims-22-147/rc).

Methods

3D-printing material

Four different photosensitive resins were readily available for consideration: transparent resin, high-toughness resin, pure white resin, and high temperature–resistant resin. The material used for phantom printing was required to meet the following criteria: (I) no strong X-ray attenuation, (II) uniform density in printed form, (III) excellent resistance to bending and fatigue, (IV) no pores or burrs, and (V) low cost.

The transparent resin and the pure white resin were excluded because of their low strength, and the high temperature–resistant resin was excluded for its high price. The high-toughness photosensitive resin material (Somos EvoLVe 128, DSM Biomedical, Geleen, The Netherlands) was ultimately found to be the best option.

For the material mechanics test, a standard dumbbell-shaped spline was made from high-toughness resin sample pieces. At room temperature, the tensile speed was set to 1 mm/min by a universal laboratory machine (8872, Instron, Boston, MA, USA), and the tensile performance was tested in accordance with ISO 527-2 (20). We analyzed the influence of 3 different printing directions and different curing times on the tensile property of the 3D-printed material.

For scanning electron microscopy (SEM) analysis, a standard dumbbell-shaped spline made of high-toughness resin was cut into a brittle fracture with a scalpel along the vertical direction of the mechanical stretching under liquid nitrogen cooling. Prior to observation, the section was coated with a gold film for 60 s. An electron microscope (S-4800, Hitachi, Tokyo, Japan) was used to observe section morphology. A section analysis was conducted to determine whether there were any defects or pores in the phantom.

Patient case selection

The study was conducted in accordance with the Declaration of Helsinki (as revised in 2013). The study was approved by the Ethics Committee of Shanghai Ninth People's Hospital (No. SH9H-2021-T67-2), and individual consent for this retrospective analysis was waived. Two patients with pelvic bone tumors who underwent surgical resection were retrospectively enrolled in this study. These 2 patients were diagnosed as type I osteochondroma and type II and III chondrosarcoma, according to Enneking's classification system, respectively. The preoperative CT exam of the pelvises was completed within 1 month before surgery. The size of the tumor was measured in transverse, sagittal, and coronal directions of the reconstructed 3D images. The size and circumference of the pelvises were measured at the level of the anterior superior iliac spine on transverse images. For detailed patient characteristics, see *Table 1*.

Phantom design

The phantom was designed with 2 main parts: a water base and a cylindrical insert. The water base simulated the shape and size of the pelvic, and the cylindrical insert was designed to be able to fit the tumor sample. The phantoms were 3D printed by a stereolithography 3D printer (Lite600, UnionTech, Shanghai, China) with high-toughness photosensitive resin. Printer parameters included a thickness of 0.1 mm and a travel speed of 8.0 m/s. After printing, the phantoms were cleaned in 98% ethanol for 15 min and then cured in an ultraviolet chamber with a wavelength of 355 nm for 60 min. Finally, we removed the support and checked the accuracy of the assembly. *Figure 1* shows the workflow we followed to produce the 3D-printed phantom from CT data.

The surgically extracted tumor specimen, in a fresh state, was put into the cylindrical insert of the phantom. The extra space within the insert was next filled up with a saline solution, and then the insert was placed inside the cylindrical water base, as shown in *Figure 2*. The 2

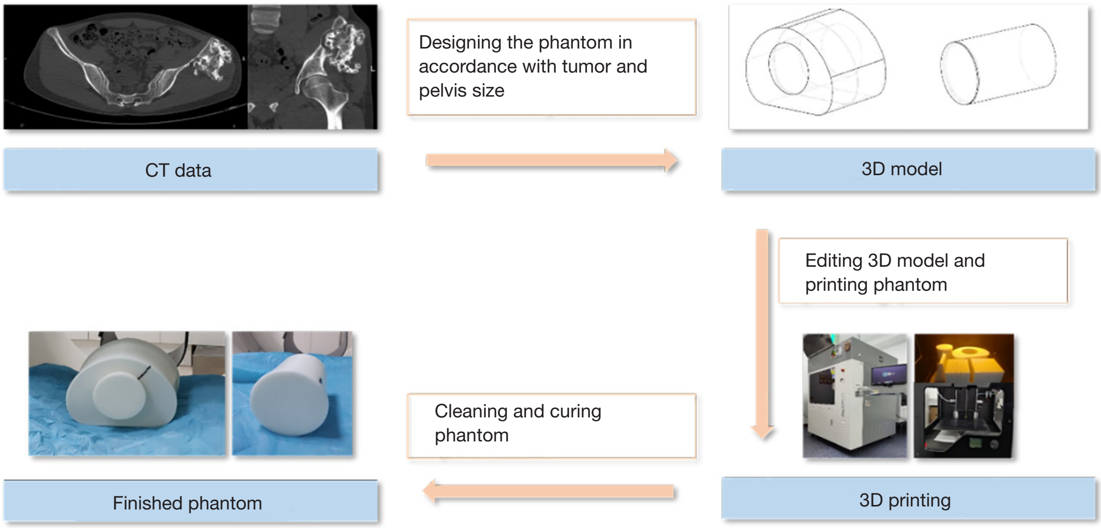

Figure 1 The workflow for producing the 3D-printed phantom from CT data. 3D, three-dimension; CT, computed tomography.

Figure 2 Assembly of the 3D-printed phantom. (A) The specimen placed into the insert. (B) The phantom assembly. (C) CT scanning of the 3D printed phantom. 3D, three-dimension; CT, computed tomography.

phantoms corresponding to each of the 2 patient cases were named phantom A and phantom B, respectively.

Imaging properties test

All CT imaging studies were performed on a 64-row CT scanner (uCT 760, United Imaging Healthcare, Shanghai, China). All CT images were reconstructed with hybrid iterative reconstruction (KARL 3D, United Imaging Healthcare, Shanghai, China) at a 1.0-mm slice thickness and 1.0-mm increments with a medium-smooth soft-tissue kernel.

The same scanning parameters were used on phantom A to assess the imaging properties of the phantom in routine pelvic CT examination, along with the following: 140 kVp tube voltage, 240 mAs reference tube current with automatic modulation, 40 mm beam collimation, 0.5 s rotation time, and 1.0 helical pitch. The tumor specimen was first scanned in the air and then scanned as part of the phantom.

The difference between the phantom image and the patient image was evaluated in terms of CT value, image noise, signal to noise ratio (SNR), and contrast to noise ratio (CNR). The image noise was defined by the standard deviation (SD) of the mean CT value within the region of interest (ROI). One radiologist with 8 years of diagnostic experience measured the mean and SD of CT value in the ROIs (area of 2 mm^2) within the neighborhood of the tumor

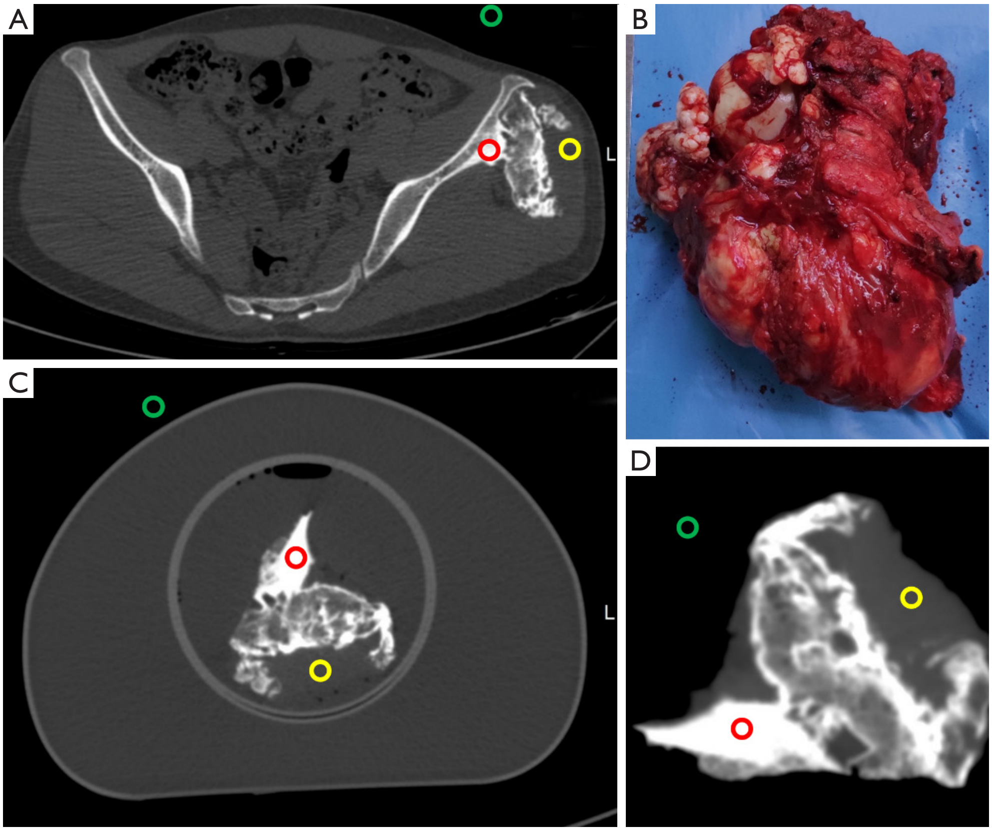

Figure 3 Typical images of a pelvic bone tumor. (A) CT images of a patient with a pelvic bone tumor. (B) Bone tumor specimen extracted in surgery. (C) CT image of the phantom with the tumor specimen placed inside. (D) CT image of the specimen placed in the air. The green circle represents the region of interest used for measuring background noise. The red and yellow circles represent the regions of interest used to measure the CT value and noise in bone and soft tissue, respectively. CT, computed tomography.

body: 1 on the cortical bone and 1 on the soft tissue. An extra ROI was placed on the background (air) for measuring background noise. *Figure 3* illustrates the location of the ROIs. Each area was measured 6 times in adjacent slices. The SNR in each ROI was calculated as follows:

$$SNR = \frac{\mu}{SD} \qquad [1]$$

The CNR between the bone and the soft tissue was calculated as follows:

$$CNR = \frac{\mu_{bone\ tissue} - \mu_{soft\ tissue}}{SD_{soft\ tissue}} \qquad [2]$$

where the μ and the SD represent the mean CT value and noise of the ROI, respectively.

Imaging protocol assessment

To determine the optimal pelvic CT protocol for detection and diagnosis of a pelvic bone tumor, repeated CT examinations of phantom B were performed on the same CT scanner mentioned above. This was done to optimize image quality and radiation dose by researching the influence of tube voltage, tube current, and pitch value and was achieved with a 3-step approach. In series 1 protocols, tube current modulation was on, and the pitch was fixed to 1.0, while different tube voltages of 80, 100, 120, and 140 kVp were chosen. In series 2 protocols, 140-kVp tube voltage and 1.0 pitch were used, while a fixed tube current was applied in a range of 80–200 mAs and a step of 40 mAs. In series 3 protocols, tube current modulation was on, and tube voltage was set to 140 kVp, while different pitch values of 0.5, 0.8, 1.1, and 1.4 were chosen. The routine

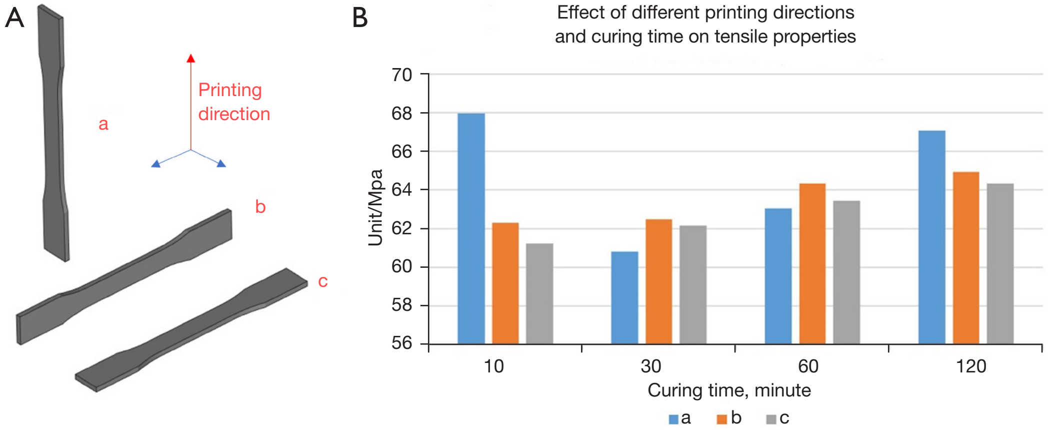

Figure 4 Influence of printing directions and curing times on the tensile property of the 3D-printed material. (A) Three different printing directions for dumbbell-shaped standard splines. (B) The effect of different printing directions and curing time on mechanical properties of 3D-printed dumbbell-shaped standard splines with high-toughness photosensitive resin. 3D, three-dimension.

pelvic CT protocol, with a 140 kVp and 240 mAs reference tube current under modulation, and a helical pitch of 1.0, was taken as the reference. This resulted in a total of 13 datasets. The objective measurements were obtained with the same approach mentioned in the "Imaging properties test" section.

Statistical analysis

SPSS software version 22.0 (IBM, Armonk, NY, USA) was used for all statistical analyses. Continuous data were analyzed for normality using the Shapiro-Wilk normality test. We used a paired *t*-test when the data were normally distributed. When the assumption of normality was not satisfied, we used the Wilcoxon matched-pairs signed-rank test. In the imaging properties test section, the CT value, image noise, SNR, and CNR of 2 images for the specimen, 1 in the air and 1 in the phantom, were compared to the patient image. In the imaging protocol assessment section, the CT value, image noise, SNR, and CNR of all 3 series of images were compared against those of the reference image. A P value <0.05 was considered statistically significant.

Results

Mechanical properties

The printed parts with high-toughness photosensitive resin differed between 1–7 Mpa under the same curing time and different printing directions. Compared with the tensile strength of the material itself at 60 MPa, the effect of different printing directions on the mechanical properties of printed dumbbell-shaped splines was negligible. With the increase in curing time, the influence of curing time on the mechanical properties of the dumbbell-shaped splines increased gradually. However, when the curing time increased to 120 min, the color of the material turned yellow, and there was the possibility of excessive aging. Therefore, the curing time of 60 min was found to be a reasonable choice (*Figure 4*).

The section of the dumbbell-shaped spline of high-toughness photosensitive resin was analyzed. When the magnification bar was 100 microns, SEM analysis showed that the fracture section was wavy, uniformly distributed, and piled up in several layers. The lamellar fracture was more obvious after being magnified 5 times (20 microns). The lamellar fracture was orderly, indicating that the oligomer copolymerization and the cross-linked structure were composed of the lamellar structure with lower molecular weight, which indicated there were no defects or pores in the phantom (*Figure 5*).

Phantom parameters

The phantom was made from high-toughness photosensitive resin, including the cylindrical water base and the cylindrical insert. The 3D-printed part of the 2 phantoms weighed about 2.3 and 2.5 kg, respectively. The diameter of the cylindrical insert was 10 cm. The printing time was about 12 hours for each phantom. The price of all materials added up to about $125 US dollars.

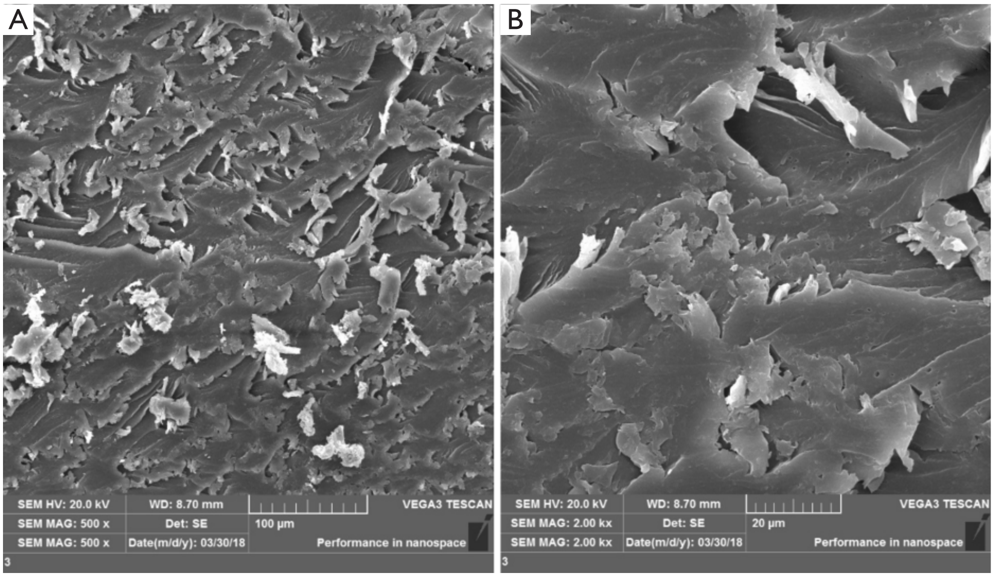

Figure 5 Scanning electron microscopy on 1 section of the 3D-printed dumbbell-shaped standard spline. (A) 100 microns magnification. (B) 20 microns magnification. 3D, three-dimension.

Table 2 Imaging properties measurements from CT images of the patient with a pelvic bone tumor, the tumor specimen placed in the air, and the proposed phantom

Imaging properties measurements	Patient image	Specimen image	Phantom image
Background noise	5.17±3.31	1.28±0.55 (P=0.046)	3.00±1.41 (P=0.071)
Bone tissue			
CT value	1,197.00±17.58	1,349.83±20.99 (P<0.001)	1,216.17±2.48 (P=0.054)
SNR	85.98±56.60	123.05±25.10 (P=0.246)	126.52±19.76 (P=0.170)
Soft tissue			
CT value	73.17±8.35	73.00±8.97 (P=0.978)	71.67±9.18 (P=0.622)
SNR	12.01±6.64	18.01±4.28 (P=0.158)	13.13±6.00 (P=0.815)
CNR	185.82±104.66	315.05±57.76 (P=0.088)	212.97±102.23 (P=0.720)

CT, computed tomography; SNR, signal to noise ratio; CNR, contrast to noise ratio.

Comparison of imaging properties

Table 2 lists the objective measurement results on images of the patient, the tumor specimen placed in the air, and the phantom. A statistically significant difference was found between the patient image and the image of the specimen in the air for the mean CT value of bone tissue (P<0.001) and the background noise (P=0.046). In the comparison between the patient image and the phantom image, there were no statistically significant differences in bone tissue (P=0.054) and soft tissue (P=0.622) CT values or in background noise (P=0.071). CT images of the phantom showed a higher SNR of bone tissue (P=0.170) and soft tissue (P=0.815) and higher CNR (P=0.720) than images of the patient, but there was no statistical difference.

Imaging protocol optimization

Figure 6 shows the comparison between images acquired with different pelvic CT protocols. Series 1 showed that the overall visibility of the pelvic bone tumor was not affected by changing the tube voltages although images

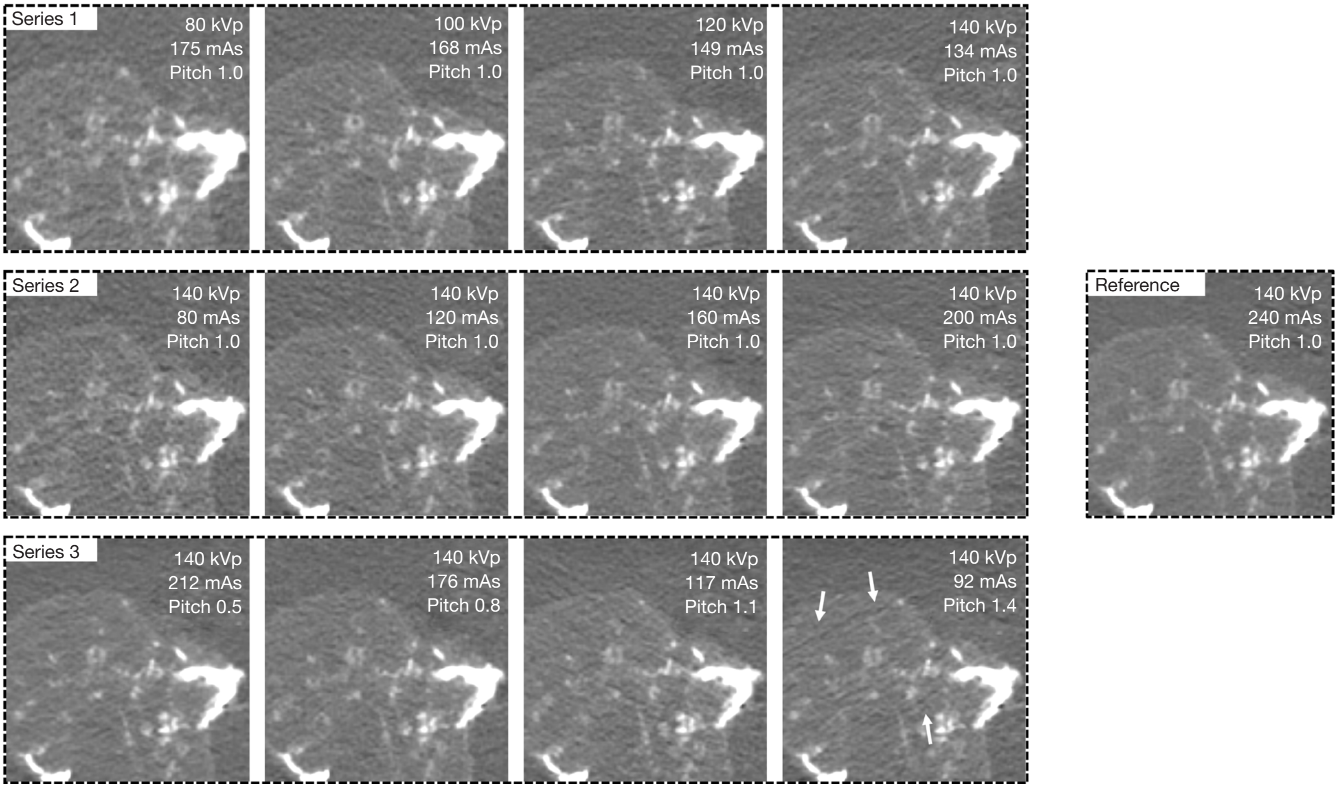

Figure 6 Enlarged view of the bone tumor in images of the phantom acquired with different pelvic CT protocols. The white arrows indicate the irregular streak artifacts on soft tissue. The display window width/window level was 300/40 HU for all images. CT, computed tomography.

with 80 and 100 kVp protocols were slightly noisier. The visual difference introduced by the varied tube current, as presented in series 2, was not noticeable. As shown in series 3, the details of the pelvic bone tumor were not affected by raising the pitch from 0.5 to 1.1. However, irregular streak artifacts on soft tissue started to appear when a high spiral pitch (1.4) was applied.

Table 3 shows image quality measurements with different pelvic CT protocols and the associated radiation dose. The dose was presented in volume CT dose index (CTDIvol), dose-length product (DLP), and the effective dose. In series 1, the CT value of bone tissue was significantly higher in images acquired with 80, 100, and 120 kVp than that in the reference image (P<0.001; P<0.001; P<0.001). The image noise of soft tissue in images acquired with 80 and 100 kVp was significantly higher than that in the reference image (P=0.011; P=0.010), leading to reduced SNR (P=0.032; P=0.042). There was no significant difference among measurements across series 2 protocols regardless of the tube current. In series 3, the pitch 1.4 image showed significantly lower SNR on soft tissue and lower CNR than did the reference image (P=0.007; P=0.014), which was due to the significantly higher image noise (P=0.018). Compared with the reference image, no significant difference was shown by images acquired with a pitch from 0.5 to 1.1.

The radiation dose was reduced by 44–86% when the tube voltage was lowered from 140 to 80 kVp, by 17–67% when the tube current was lowered from 240 to 80 mAs, and by 12–61% when the pitch was raised from 0.5 to 1.4. Given the difference in CT value and SNR, dose reduction using a lower tube voltage is not recommended. Without compromising CT value, noise, SNR, and CNR, the protocol with the 80 mAs tube current in series 2 received the lowest radiation dose, which was a reduction of 67% when compared to the reference protocol. The optimal CT protocol for pelvic tumor diagnosis might be found with a reduced tube current as low as 80 mAs or an increased helical pitch under 1.4 while keeping tube voltage at 140 kVp.

Table 3 Measurements in images acquired with different pelvic CT protocols and the associated radiation dose

CT protocols	kVp	mAs	Pitch	Bone tissue			Soft tissue				Radiation dose		
				CT value	Noise	SNR	CT value	Noise	SNR	CNR	CTDIvol (mGy)	DLP (mGy cm)	Effective dose (mSv)
Reference	140	240	1	1,008.78±38.06	20.77±2.85	49.38±6.11	33.85±4.16	12.23±2.79	2.91±0.75	83.78±18.51	29.83	881.75	13.23
Series 1	80	175	1	1,410.48±64.34 (P<0.001)	24.70±8.34 (P=0.348)	65.77±27.02 (P=0.216)	36.57±5.05 (P=0.476)	18.57±2.79 (P=0.011)	1.97±0.10 (P=0.032)	75.24±8.56 (P=0.318)	4.08	120.59	1.81
	100	168	1	1,237.57±42.39 (P<0.001)	24.22±7.53 (P=0.472)	64.09±42.52 (P=0.509)	35.28±2.61 (P=0.589)	18.40±2.30 (P=0.010)	1.95±0.26 (P=0.042)	66.31±8.02 (P=0.105)	8.32	246.14	3.69
	120	149	1	1,080.32±42.22 (P<0.001)	19.63±4.47 (P=0.547)	58.76±16.78 (P=0.202)	32.27±3.09 (P=0.475)	15.77±2.94 (P=0.078)	2.14±0.55 (P=0.099)	69.44±16.50 (P=0.164)	12.44	368.09	5.52
	140	134	1	1,009.43±35.12 (P=0.871)	20.07±5.58 (P=0.714)	54.75±16.23 (P=0.369)	31.37±1.86 (P=0.102)	12.93±4.21 (P=0.786)	2.74±1.00 (P=0.759)	84.19±26.76 (P=0.982)	16.59	490.88	7.36
Series 2	140	80	1	1,016.03±36.08 (P=0.472)	19.13±9.76 (P=0.748)	67.40±29.44 (P=0.248)	33.05±4.44 (P=0.811)	13.53±5.37 (P=0.728)	3.11±1.95 (P=0.871)	86.61±38.57 (P=0.914)	9.94	294.14	4.41
	140	120	1	1,016.12±46.76 (P=0.306)	19.95±7.68 (P=0.805)	62.48±32.91 (P=0.397)	31.47±4.17 (P=0.347)	13.37±1.54 (P=0.347)	2.41±0.57 (P=0.056)	74.55±8.07 (P=0.275)	14.92	441.5	6.62
	140	160	1	1,000.63±38.30 (P=0.249)	20.92±8.35 (P=0.963)	64.33±43.89 (P=0.443)	31.53±1.08 (P=0.273)	12.83±3.23 (P=0.629)	2.59±0.54 (P=0.276)	79.61±17.30 (P=0.400)	19.89	588.57	8.83
	140	200	1	998.60±43.31 (P=0.162)	20.55±3.95 (P=0.864)	50.8±12.29 (P=0.755)	31.48±6.76 (P=0.593)	11.57±2.98 (P=0.417)	2.93±0.98 (P=0.953)	88.79±20.24 (P=0.524)	24.83	734.75	11.02
Series 3	140	212	0.5	1,012.40±38.98 (P=0.619)	18.78±8.86 (P=0.641)	71.28±38.77 (P=0.24)	30.68±3.00 (P=0.316)	9.70±2.56 (P=0.222)	3.36±0.74 (P=0.309)	109.54±32.23 (P=0.209)	26.37	772.84	11.59
	140	176	0.8	1,013.23±46.41 (P=0.620)	20.00±4.59 (P=0.770)	53.46±12.90 (P=0.540)	30.58±6.07 (P=0.485)	12.95±6.22 (P=0.807)	2.91±1.14 (P=0.990)	105.76±64.30 (P=0.502)	21.91	644.92	9.67
	140	117	1.1	1,018.32±39.03 (P=0.399)	20.87±9.72 (P=0.979)	57.83±20.57 (P=0.303)	30.27±5.62 (P=0.375)	13.53±3.41 (P=0.581)	2.36±0.68 (P=0.302)	77.84±19.86 (P=0.683)	14.59	432.85	6.49
	140	92	1.4	1,000.03±32.79 (P=0.403)	21.37±1.86 (P=0.683)	47.23±5.06 (P=0.524)	30.08±4.90 (P=0.066)	20.2±4.61 (P=0.018)	1.57±0.42 (P=0.007)	51.68±17.12 (P=0.014)	11.46	341.58	5.12

CT, computed tomography; SNR, signal to noise ratio; CNR, contrast to noise ratio; CTDIvol, volume CT dose index; DLP, dose-length product.

Discussion

Our results demonstrate that personalized pelvic phantoms printed with high-toughness photosensitive resin material combined with postoperative fresh tumor specimens could be used to simulate the pelvic environment of patients in CT imaging studies.

In terms of physical properties, the 3D-printed water base showed uniform modulus, excellent bending strength, and homogeneous X-ray attenuation. In preparing the medical phantom, it is often necessary to select different materials and processing methods according to the tested phantom's different equipment and imaging requirements so that the final phantom can meet the corresponding requirements (11). The 3D-printing technology has its advantage in rapid prototyping and is often used for custom design (21). Many materials are used for 3D printing. Some researchers found that the high-toughness photosensitive resin had low porosity, low water absorption, excellent bending resistance, and good fatigue resistance (22). In this study, high-toughness photosensitive resin materials were used for phantom printing. SEM of the dumbbell-shaped spline showed that the phantom was composed of a low molecular weight structure with a whole-flake shape, which proved that there were no defects or pores inside the phantom. Accordingly, the printed phantom part had a dense structure and was waterproof.

In the imaging properties test, the CT values of bone and soft tissue and the noise measured in regions relative to the bone tumor specimen within the 3D-printed phantom were consistent with those in preoperative CT images of pelvic bone tumor patients. The CT value reflects the X-ray attenuation coefficient and the density of different tissues. The ideal phantom has a CT value of the basic anatomical structure that is close to that of the corresponding human body. In this study, the size and shape of the pelvis was the main consideration in designing the phantom. The size of the water base was determined accordingly to obtain consistent overall CT attenuation. Such a phantom design was not patient-specific, particularly on interior structures surrounding the tumor. This is worth exploring in a future study.

In the imaging protocol assessment, our study showed the feasibility of using low-dose pelvic CT protocols to detect and diagnose a pelvic bone tumor while maintaining acceptable image quality. We tested different pelvic CT protocols comprising a range of tube voltage, tube current, and pitch values. Quantitative image quality measurement showed no significant differences when the tube current was lowered from 240 to 80 mAs or when the pitch was increased from 0.5 to 1.1. A low tube current or high pitch CT protocol is available with high-speed CT scanners and has strong potential to achieve dose reduction. In theory, reducing the tube current and increasing the pitch during CT scans are accompanied by increased image noise and compromised spatial resolution. However, within the investigated range, this study did not find them to be a critical issue.

The development and application of the 3D-printing phantom offer an alternative approach for imaging investigations in a safe and controlled environment. Such phantoms can be kept and reused over a longer period. Radiation dosage does not present an ethical dilemma when using a CT phantom compared to testing real patients. However, future studies might be interested in determining whether such a phantom would be sufficient for studying multiple types of tumors, such as intrapelvic soft tissue tumors and solid organ tumors. Compared to primary bone tumors, these tumors have lower mean CT attenuation and lower contrast to surrounding tissues, posing further challenges for CT protocol optimization.

Conclusions

This study demonstrated that a CT phantom with fresh pathological tissues could be designed and produced via 3D printing. The 3D-printed phantom can simulate the radiological properties of pelvic tumors and be successfully used in imaging studies of pelvic bone tumors. According to the preliminary findings, a low-dose pelvic CT protocol with acceptable image quality is achievable through use of a reduced tube current or increased pitch.

Acknowledgments

Funding: This work was supported by funds from the National Natural Science Foundation of China (No. 82171993), the Clinical Research Plan of SHDC (No. SHDC2020CR3083B), and the Technology Project of Shanghai Science and Technology Commission (No. 19441902700).

Footnote

Reporting Checklist: The authors have completed the MDAR checklist. Available at https://qims.amegroups.com/article/view/10.21037/qims-22-147/rc

Conflicts of Interest: All authors have completed the ICMJE uniform disclosure form (available at https://qims.amegroups.com/article/view/10.21037/qims-22-147/coif). YZ and GZ are current employees of United Imaging Healthcare, Shanghai, China. The other authors have no conflicts of interest to declare.

Ethical Statement: The authors are accountable for all aspects of the work in ensuring that questions related to the accuracy or integrity of any part of the work are appropriately investigated and resolved. The study was conducted in accordance with the Declaration of Helsinki (as revised in 2013). This study was approved by Ethics Committee of Shanghai Ninth People's Hospital (No. SH9H-2021-T67-2), and individual consent for this retrospective analysis was waived.

References

1. Fujiwara T, Medellin Rincon MR, Sambri A, Tsuda Y, Clark R, Stevenson J, Parry MC, Grimer RJ, Jeys L. Limb-salvage reconstruction following resection of pelvic bone sarcomas involving the acetabulum. Bone Joint J 2021;103-B:795-803.
2. Qu Y, Li X, Yan Z, Zhao L, Zhang L, Liu C, Xie S, Li K, Metaxas D, Wu W, Hao Y, Dai K, Zhang S, Tao X, Ai S. Surgical planning of pelvic tumor using multi-view CNN with relation-context representation learning. Med Image

Anal 2021;69:101954.

3. Luo Z, Li J, Qin G, Zeng H, He Z, Pan D, Li Y, Chen W, Shen X. Clinical and imaging features of 112 patients with irregular and flat bone osteosarcoma. Quant Imaging Med Surg 2022;12:1988-2001.
4. Xu L, Yang P, Hu K, Wu Y, Xu-Welliver M, Wan Y, Luo C, Wang J, Wang J, Qin J, Rong Y, Niu T. Prediction of neoadjuvant chemotherapy response in high-grade osteosarcoma: added value of non-tumorous bone radiomics using CT images. Quant Imaging Med Surg 2021;11:1184-95.
5. Takenaka S, Tamiya H, Wakamatsu T, Nakai S, Imura Y, Outani H, Yagi T, Kawai A. Impact of Surgical Resection and Reasons for Poor Prognosis of Pelvic Osteosarcoma Based on the Bone Tumor Registry in Japan. Cancers (Basel) 2021;13:3320.
6. Toia GV, Mileto A, Wang CL, Sahani DV. Quantitative dual-energy CT techniques in the abdomen. Abdom Radiol (NY) 2021. doi: 10.1007/s00261-021-03266-7.
7. Tabari A, Gee MS, Singh R, Lim R, Nimkin K, Primak A, Schmidt B, Kalra MK. Reducing Radiation Dose and Contrast Medium Volume With Application of Dual-Energy CT in Children and Young Adults. AJR Am J Roentgenol 2020;214:1199-205.
8. Pawałowski B, Szweda H, Dudkowiak A, Piotrowski T. Quality evaluation of monoenergetic images generated by dual-energy computed tomography for radiotherapy: A phantom study. Phys Med 2019;63:48-55.
9. van Hamersvelt RW, Schilham AMR, Engelke K, den Harder AM, de Keizer B, Verhaar HJ, Leiner T, de Jong PA, Willemink MJ. Accuracy of bone mineral density quantification using dual-layer spectral detector CT: a phantom study. Eur Radiol 2017;27:4351-9.
10. Jahnke P, Schwarz FB, Ziegert M, Almasi T, Abdelhadi O, Nunninger M, Hamm B, Scheel M. A radiopaque 3D printed, anthropomorphic phantom for simulation of CT-guided procedures. Eur Radiol 2018;28:4818-23.
11. Watanabe Y, Constantinou C. Phantom Materials in Radiology. 2006. Available online: https://experts.umn.edu/en/publications/phantom-material-for-radiology
12. Servomaa A, Björkman J. Use of an AAPM (American Association of Physicists in Medicine) DSA phantom in quality assurance. Eur J Radiol 1989;9:217-20.
13. Chotas HG, Floyd CE Jr, Johnson GA, Ravin CE. Quality control phantom for digital chest radiography. Radiology 1997;202:111-6.
14. Xu XG, Chao TC, Bozkurt A. VIP-Man: an image-based whole-body adult male model constructed from color photographs of the Visible Human Project for multi-particle Monte Carlo calculations. Health Phys 2000;78:476-86.
15. Huston J 3rd, Muhm JR. Solitary pulmonary nodules: evaluation with a CT reference phantom. Radiology 1989;170:653-6.
16. Xu XG. An exponential growth of computational phantom research in radiation protection, imaging, and radiotherapy: a review of the fifty-year history. Phys Med Biol 2014;59:R233-302.
17. Hao Y, Luo D, Wu J, Wang L, Xie K, Yan M, Dai K, Hao Y. A novel revision system for complex pelvic defects utilizing 3D-printed custom prosthesis. J Orthop Translat 2021;31:102-9.
18. Xu L, Qin H, Tan J, Cheng Z, Luo X, Tan H, Huang W. Clinical study of 3D printed personalized prosthesis in the treatment of bone defect after pelvic tumor resection. J Orthop Translat 2021;29:163-9.
19. Niebuhr NI, Johnen W, Güldaglar T, Runz A, Echner G, Mann P, Möhler C, Pfaffenberger A, Jäkel O, Greilich S. Technical Note: Radiological properties of tissue surrogates used in a multimodality deformable pelvic phantom for MR-guided radiotherapy. Med Phys 2016;43:908-16.
20. ISO 527-2:2012. Plastics-Determination of Tensile Properties-Part 2: Test Conditions for Moulding and Extrusion Plastics. Geneva, Switzerland: International Organization for Standardization, 2012.
21. Li B, Yu L, Huang Z, Liang Y, Li G, Zhao Y. A novel device for treatment of osteonecrosis of femoral head: Feasibility and preliminary efficacy of animal study. J Orthop Translat 2021;31:20-5.
22. Melchels FP, Feijen J, Grijpma DW. A review on stereolithography and its applications in biomedical engineering. Biomaterials 2010;31:6121-30.

Cite this article as: Li X, Wu B, Zou Y, Zhang G, Liu S, Zhao L, Zhang Z, Wu W, Liu C, Ai S. Development of a 3D-printed pelvic CT phantom combined with fresh pathological tissues of bone tumor. Quant Imaging Med Surg 2022;12(9):4647-4657. doi: 10.21037/qims-22-147